Composites Part B 324 (2026) 113877

Contents lists available at ScienceDirect

Composites Part B

journal homepage: www.elsevier.com/locate/compositesb

Hydrophobic CNF/MXene composite aerogels with synergistic structure–interface engineering for reliable flexible sensing

Ao Li [a,b], Jun Xu [a,c,*], Dezhong Xu [d], Zhaohui Zhang [a], Shengtao Zhou [a], Hanyuan Chen [b], Kefu Chen [a], Mizi Fan [b,**]

[a] State Key Laboratory of Advanced Papermaking and Paper-based Materials, Plant Fiber Materials Science Research Center, South China University of Technology, Guangzhou, 510640, China
[b] College of Engineering, Design and Physical Sciences, Brunel University London, UB8 3PH, UK
[c] Guangdong Key Laboratory of Plant Resources Biorefinery, Guangzhou, 510006, China
[d] College of Biomass Science and Engineering, Sichuan University, Chengdu, 610065, China

ARTICLE INFO

Keywords:
Cellulose nanofibers
Composite aerogels
Flexible pressure sensing
Ordered porous structure

ABSTRACT

Flexible piezoresistive aerogels are promising for wearable electronics and sensing in complex environments, yet their practical application is often limited by structural collapse during compression and moisture-induced conductive instability. Herein, an ultralight hydrophobic CNF/MXene composite aerogel is developed through synergistic structure–interface engineering. Directional freeze-casting creates vertically aligned lamellar channels that effectively confine compressive deformation and guide the assembly of MXene into continuous conductive pathways. Meanwhile, in situ vapor-phase deposition of methyltrichlorosilane (MTS) establishes a stable hydrophobic interface that suppresses moisture-induced softening and conductive fluctuations. Benefiting from the synergy between ordered structural regulation and interfacial stabilization, the resulting aerogel exhibits an ultralow density of 1.7 mg cm^{-3}, a water contact angle of 146.1°, and a high sensitivity of 438.65 kPa^{-1} over 0-98 kPa, together with stable operation over 1000 compression cycles. Reliable sensing performance is maintained under coupled high-temperature, high-humidity, and dynamic compression conditions. In addition, the aerogel demonstrates rapid photothermal conversion capability, reaching 179.6°C under light irradiation. This work provides a practical strategy for constructing environmentally reliable porous conductive aerogels and offers new insights into the cooperative regulation of deformation behavior and interfacial stability for flexible sensing applications.

1. Introduction

With the rapid development of flexible wearable electronics, intelligent human–machine interaction, and health-monitoring technologies, piezoresistive sensors capable of stably converting external mechanical stimuli into electrical signals have attracted widespread attention [1,2]. Compared with capacitive or piezoelectric devices, piezoresistive sensors offer the advantages of simple device architecture, convenient signal readout, and easy system integration, thereby showing broad application prospects in scenarios such as motion recognition, pulse monitoring, and sensing under complex environmental conditions [3,4]. However, flexible sensors for practical applications are expected not only to provide high sensitivity and wide detection ranges, but also to maintain stable and reproducible electrical outputs under repeated deformation and complex environmental conditions. This challenge is particularly pronounced in porous piezoresistive materials, where highly porous architectures enable large deformation responses but often lead to pore-wall collapse, unstable conductive contacts, and signal drift during cyclic compression [5]. Therefore, simultaneously achieving high sensitivity, structural robustness, and environmental adaptability remains a major challenge for porous flexible sensing systems.

To address the conductivity requirement of such devices, various highly conductive nanomaterials, including graphene, carbon

* Corresponding author. State Key Laboratory of Advanced Papermaking and Paper-based Materials, Plant Fiber Materials Science Research Center, South China University of Technology, Guangzhou, 510640, China.
** Corresponding author.
E-mail addresses: Xujun@scut.edu.cn (J. Xu), Mizi.Fan@brunel.ac.uk (M. Fan).

https://doi.org/10.1016/j.compositesb.2026.113877
Received 30 April 2026; Received in revised form 30 May 2026; Accepted 5 June 2026
Available online 5 June 2026

nanotubes, and MXene, have been introduced to construct responsive conductive networks. Among them, MXene has emerged as a particularly promising building block because of its metallic conductivity, abundant surface terminations, and favorable interfacial processability [6,7]. Integrating MXene with elastomers, sponges, hydrogels, and lightweight porous scaffolds has been shown to markedly enhance sensitivity, low-pressure responsiveness, and multifunctional integration in flexible sensors [8,9]. In biomimetic lamellar structures and porous aerogels, MXene can effectively construct continuous conductive pathways for pressure-responsive sensing. For example, Ren et al. developed a biomimetic lamellar silicon nanofiber/MXene aerogel sensor inspired by avian-bone microstructures, in which a lamella–pillar cooperative architecture enabled effective decoupling of pressure and temperature signals, together with excellent recovery and high sensing resolution [10]. Nevertheless, MXene nanosheets in porous aerogels still tend to restack or locally disconnect during drying and repeated deformation, leading to conductive-network instability [11]. More importantly, the intrinsically hydrophilic nature of MXene and cellulose-based frameworks makes these systems highly vulnerable to moisture-induced interfacial softening and conductivity attenuation under humid conditions [12]. Although previous studies have significantly improved the sensing performance of MXene-based porous materials, their long-term operational stability under complex environmental conditions remains insufficiently explored.

Notably, this issue originates not only from the conductive component itself, but also from the uncontrolled deformation of porous structures during compression and interfacial instability under environmental exposure. In conventional randomly porous aerogels, pore-wall collapse and conductive-contact evolution during compression often occur randomly, leading to poor signal reproducibility, response hysteresis, and cyclic drift [13,14]. In recent years, ordered porous architectures constructed through directional freezing, biomimetic assembly, and programmable fabrication have attracted increasing attention because they can effectively regulate deformation behavior and improve the consistency of piezoresistive responses. For example, Min et al. fabricated an anisotropic graphene aerogel with aligned lamellar channels through freeze-induced assembly, significantly improving pressure and bending sensing performance [15]. Similarly, Gao et al. developed an ultrasoft biomimetic porous material inspired by natural wood, demonstrating enhanced structural robustness and sensing stability [16]. In addition, three-dimensional printing enables the precise fabrication of designed periodic lattice structures, providing a new route for structural engineering to regulate local deformation modes and realize programmable piezoresistive behaviors [17]. These advances indicate that the improvement of sensing performance should not rely solely on increasing conductivity; more importantly, it requires coupling predictable deformation with reproducible electrical response through rational structural design [18–20]. However, ordered architectures alone are still insufficient to guarantee reliable operation under practical environmental conditions. Once moisture penetrates into the framework, interfacial softening and fluctuations in conductive pathways can still undermine sensing stability. Therefore, achieving stable sensing performance in complex environments requires the synergistic integration of structural regulation and interfacial stabilization.

Herein, we develop a hydrophobic CNF/MXene composite aerogel through a synergistic structure–interface engineering strategy. Vertically aligned lamellar channels are first constructed by directional freezing, followed by in situ vapor-phase deposition of methyltrichlorosilane (MTS) to establish a stable hydrophobic interface throughout the porous framework. The aligned lamellar channels not only provide high compressibility, but also guide MXene assembly along the pore walls to form continuous conductive pathways for stable pressure-responsive sensing. Subsequent MTS deposition preserves the integrity of the porous structure while creating a stable hydrophobic interface on the channel surfaces, effectively suppressing moisture-induced structural softening and electrical instability. Benefiting from the synergy between ordered structural regulation and interfacial stabilization, the resulting aerogel exhibits excellent sensing stability and reproducibility under cyclic compression and humid conditions, while also retaining the characteristic photothermal response of MXene. This work provides an effective strategy for constructing environmentally stable porous conductive aerogels and offers new insights into the cooperative regulation of structural deformation and interfacial stability for flexible sensing applications.

2. Results and discussion

2.1. Structural–interfacial synergistic design and mechanistic basis of the CMM aerogel

Conventional porous conductive aerogels generally suffer from unstable electromechanical responses under coupled compression and humid environments. As illustrated in Fig. 1a(i), randomly porous structures undergo uncontrolled local collapse and stochastic conductive-network reconstruction during compression, leading to signal fluctuation and hysteresis. Even in aligned porous structures, moisture penetration can still disturb the conductive microenvironment and induce electrical instability without interfacial protection (Fig. 1a (ii)).

To overcome these coupled instability issues, a structural–interfacial synergistic strategy was developed by integrating directional freeze-casting with MTS vapor-phase deposition (Fig. 1b). Directional freezing guided the assembly of CNF/MXene components into vertically aligned lamellar channels, while subsequent MTS modification formed a hydrophobic siloxane interface throughout the porous framework. This combined design enabled simultaneous regulation of deformation behavior and environmental stability. At the structural level, the aligned lamellar architecture generated by directional freezing provides a more predictable deformation pathway during compression. Compared with randomly porous frameworks, the ordered channels help suppress localized collapse and stabilize conductive-network evolution. As MXene nanosheets are confined along the lamellar walls, conductive contacts change more gradually and reproducibly during loading and unloading, thereby contributing to stable piezoresistive output. At the interfacial level, MTS vapor-phase deposition forms a hydrophobic siloxane layer on the porous framework, which effectively suppresses water adsorption and moisture-induced interfacial disturbance. Together with the rough porous surface, the low-surface-energy interface enhances water repellency and helps maintain conductive-network stability under humid conditions.

Benefiting from the synergy between the aligned porous structure and stabilized hydrophobic interface, the CMM aerogel achieves reliable pressure sensing under humid conditions while maintaining rapid photothermal response (Fig. 1c). These results demonstrate the effectiveness of the proposed structural–interfacial synergistic strategy for constructing multifunctional porous conductive aerogels with enhanced environmental reliability.

2.2. Microstructural and interfacial chemical characterization of the aerogels

A CNF/MXene composite aerogel was fabricated through the synergistic assembly of CNF and exfoliated MXene nanosheets. Multiscale structural and interfacial characterizations were conducted to elucidate the assembly behavior and structural evolution of the aerogels (Fig. 2). Through directional structural regulation and interfacial engineering, the composite effectively integrates the morphological advantages and chemical functionalities of each component.

MXene was prepared from the Ti_3AlC_2 precursor by selective LiF/HCl etching followed by ultrasonic delamination [7]. TEM images (Fig. S1) reveal a typical two-dimensional flake-like morphology with well-defined sheet edges, confirming the successful exfoliation of MXene

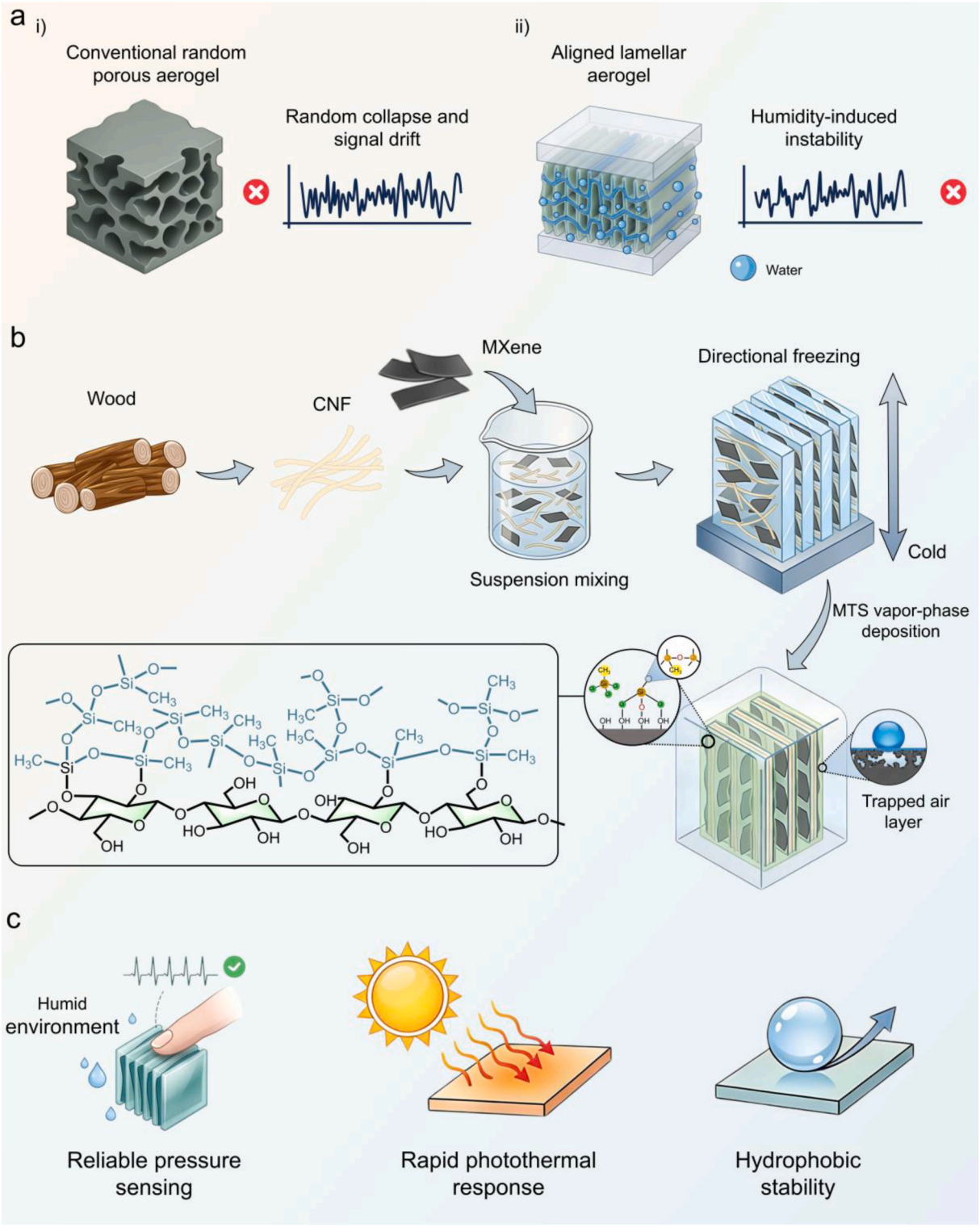

Fig. 1. Structural–interfacial synergistic design of the CMM aerogel. a) Schematic illustration of the instability of porous conductive aerogels under complex service conditions: i) random collapse and signal drift in conventional randomly porous aerogels; ii) humidity-induced instability in aligned lamellar aerogels without interfacial protection. b) Fabrication route of the CMM aerogel through CNF extraction from wood, suspension mixing with MXene, directional freezing, and subsequent MTS vapor-phase deposition, leading to the formation of a hydrophobic siloxane interface and trapped-air layer. c) Functional features of the CMM aerogel, including reliable pressure sensing in humid environments, rapid photothermal response, and hydrophobic stability.

nanosheets. AFM analysis further shows that the nanosheets possess an average thickness of approximately 2.3 nm (Fig. S2a and b) with sub-micrometre lateral dimensions, which is favorable for constructing continuous conductive pathways within the aerogel [6]. After co-dispersion with CNFs, the freeze-dried composite aerogel exhibited an ultralow density (1.7 mg cm^{-3}) and could remain stably supported on the surface of a green leaf (Fig. 2a), demonstrating its lightweight characteristic and robust three-dimensional framework. TEM

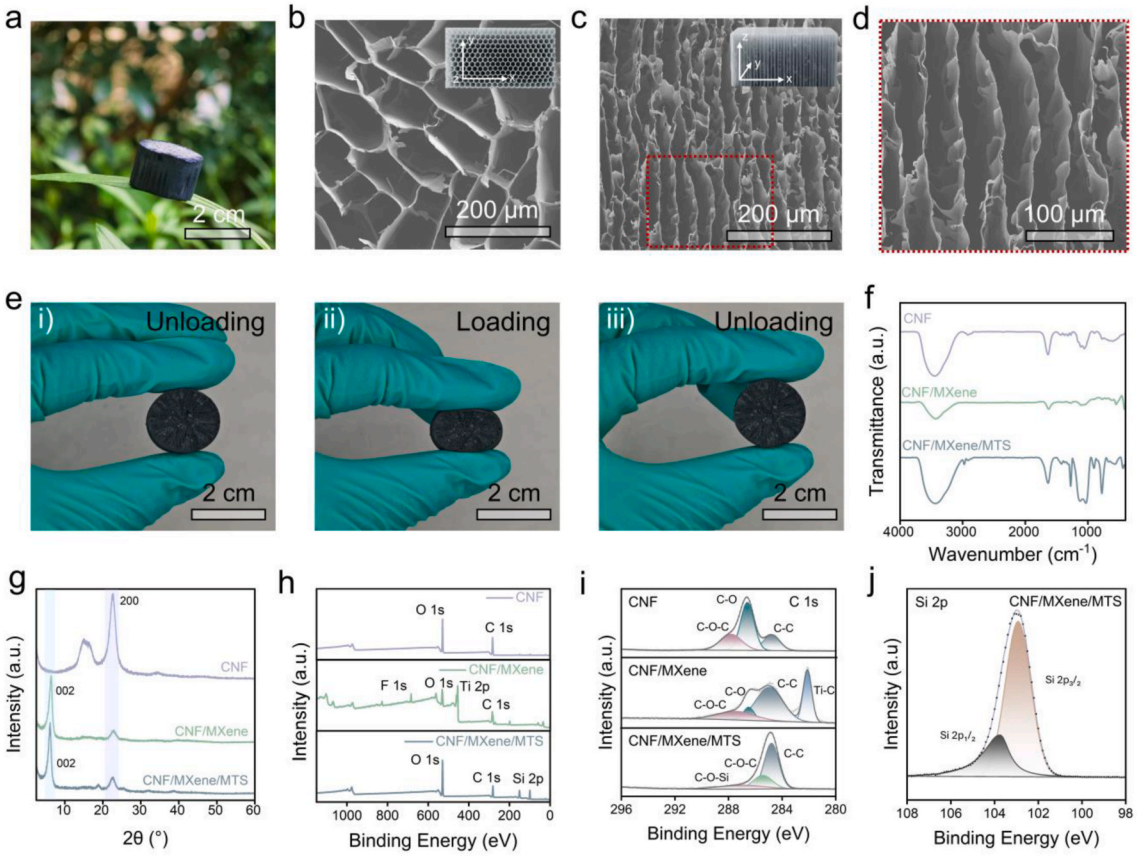

Fig. 2. Multiscale structural and interfacial chemical characterization of the CMM aerogels. a) Demonstration of the lightweight nature of the CMM aerogel, which can be stably supported on the surface of a green leaf, indicating its ultralow density. b) SEM image along the transverse plane (perpendicular to the freezing direction), revealing an interconnected cellular (honeycomb-like) network. c) SEM image along the longitudinal plane (parallel to the freezing direction), showing a distinct oriented lamellar porous architecture. d) High-magnification SEM image revealing continuous lamellar scaffolds and interlayer channels, indicating that MXene and CNF jointly constitute the composite lamellar walls. e) The aerogel retains its overall morphology after repeated compression, demonstrating good structural stability and elastic recovery capability. f) FTIR spectra. g) XRD patterns. h) XPS survey spectra. i) XPS C1s spectra. j) XPS Si2p spectra. (For interpretation of the references to colour in this figure legend, the reader is referred to the Web version of this article.)

observations (Fig. S3) reveal an entangled CNF nanofibrillar network serving as the structural scaffold for aerogel formation and MXene anchoring. The interconnected fibrillar framework provides abundant support sites for the homogeneous distribution of MXene nanosheets.

SEM images reveal a highly anisotropic porous architecture generated by directional freeze-casting. The transverse section exhibits an interconnected cellular structure, whereas the longitudinal section displays aligned lamellar channels along the freezing direction (Fig. 2b and c). High-magnification SEM images further show continuous lamellar walls with rough and wrinkled surfaces, indicating the uniform incorporation of MXene within the CNF framework (Fig. 2d). Notably, the aligned porous architecture remains well preserved after MTS treatment, indicating that the interfacial modification process does not disrupt the integrity of the lamellar framework. Macroscopically, the aerogel rapidly recovered its original shape after repeated manual compression (Fig. 2e), demonstrating excellent elasticity and structural stability. This mechanical resilience originates from the synergistic effect of the flexible CNF scaffold and reinforcing MXene nanosheets.

The FTIR spectra (Fig. 2f) reveal the interfacial chemical evolution of the aerogels. For CNF, characteristic hydroxyl-related vibrations appear at 3452 and 1632 cm^{-1}. After MXene incorporation, characteristic Ti–O/Ti–C vibrations at 551 cm^{-1} confirm MXene incorporation, while the hydroxyl-related band becomes slightly shifted and narrowed, indicating interfacial interactions between MXene nanosheets and CNF surface hydroxyl groups. Following MTS vapor-phase deposition, characteristic Si–*O*–Si and Si–CH_3 absorption bands appear at 1034 and 1270 cm^{-1}, respectively, whereas the hydroxyl-related bands are significantly attenuated, confirming the successful formation of a hydrophobic siloxane layer through silanization reactions with surface hydroxyl groups. XRD analysis (Fig. 2g) further elucidates the structural evolution during aerogel fabrication. The characteristic (200) diffraction peak of CNF remains nearly unchanged after composite formation and MTS modification, indicating that the cellulose crystalline structure is well preserved throughout the fabrication process. Meanwhile, the unchanged MXene (002) peak suggests that silane deposition occurs mainly on the framework surface without disrupting the conductive structure. In addition, no noticeable peak broadening is observed after MTS treatment, indicating that the deposited siloxane species mainly distribute on the framework surface without disturbing the original lattice structure. XPS spectra (Fig. 2h) were employed to investigate the evolution of elemental composition and interfacial chemical states. Pure CNF exhibits only C and O signals, whereas distinct Ti and F signals appear after MXene incorporation, confirming the successful integration of MXene into the composite framework. After MTS modification, a characteristic Si signal emerges while the Ti and F signals become attenuated, indicating the successful deposition of silane species on the framework surface. Fig. 2i presents the high-resolution C 1s spectra of CNF, CNF/MXene, and CNF/MXene/MTS. A characteristic Ti–C peak at approximately 281.8 eV appears after MXene incorporation. Following MTS treatment, the C–C/C–H component becomes enhanced, whereas the Ti–C signal and oxygen-containing carbon species are weakened, reflecting the formation of a silane-coated surface environment. The

corresponding O 1s spectra are shown in Fig. S4. After MXene incorporation, additional Ti–O and Ti–OH contributions appear, indicating the coexistence of oxygen-containing environments from both CNF and MXene. Following MTS modification, a distinct Si–*O*–Si component emerges while the Ti–O/Ti–OH-related signals become significantly attenuated, confirming the formation of a siloxane-derived surface layer on the CNF/MXene framework. Moreover, the Si 2p spectrum of CNF/MXene/MTS (Fig. 2j) exhibits a characteristic peak at 103 eV assigned to Si–*O*–Si species, confirming the successful construction of the siloxane interface during MTS vapor-phase deposition. These results confirm that MTS preferentially constructs a siloxane shielding interface on the CNF/MXene framework while preserving the conductive MXene network.

2.3. Hydrophobic interfacial regulation and evaluation of functional stability

MTS vapor-phase deposition was employed to regulate the interfacial wettability of the three-dimensional porous CM_4 framework (CNF: MXene mass ratio of 2:4) by forming a low-surface-energy hydrophobic layer. As the MTS dosage increased from 0 to 2.0 g, the surface wettability of the samples changed markedly, with the static water contact angle (WCA) rapidly transitioning from a hydrophilic state to a highly hydrophobic state (Fig. 3a, Fig. S5). In particular, the sample treated with 1.5 g of MTS exhibited the most effective hydrophobic modification, showing a WCA of 146.1°, indicating that an appropriate MTS dosage can effectively achieve uniform hydrophobic functionalization of the scaffold surface. This transition is mainly attributed to the hydrolysis and condensation of MTS under vapor-phase conditions, which generate a crosslinked siloxane network, while the terminal methyl groups significantly reduce the surface energy of the material. In combination with the intrinsic micro/nano hierarchical rough structure of the aerogel, these effects collectively endow the material with excellent liquid-repellent behavior, enabling droplets to maintain a stable spherical shape without readily penetrating into the scaffold interior. However, a further increase in the dosage to 2.0 g (CMM_5) resulted in a plateau and a slight decline in hydrophobicity, with the WCA dropping to 143.4°. This trend indicates that while the optimal loading ensures uniform coverage, excessive deposition leads to the saturation of reactive hydroxyl sites on the scaffold. Beyond this saturation point, redundant silane molecules tend to self-condense and agglomerate on the pore walls, which partially masks and disrupts the intrinsic micro/nano hierarchical rough structure of the aerogel, thereby slightly reducing the surface liquid repellency.

As illustrated in Fig. 3b, MTS molecules penetrate into the three-dimensional aerogel network via vapor-phase diffusion, where the reactive Si–Cl groups undergo hydrolysis and condensation with hydroxyl groups on the scaffold surface, thereby forming a siloxane-based crosslinked layer through covalent anchoring. The outward-oriented nonpolar methyl (-CH_3) groups effectively reduce the surface energy and suppress the adsorption of water molecules. The wetting behaviour of liquids with different surface tensions on the CMM_4 surface (Fig. S6), including water, black tea, coffee, milk, and human sweat, further demonstrates the broad liquid repellency of the hydrophobic interface, indicating its adaptability to multiple liquid media. For the complex three-dimensional scaffold structure, contact-angle measurements on both the outer surface and cross-section (Fig. 3c) reveal that MTS molecules can penetrate into the pore interior, forming a continuous bulk hydrophobic network from the macroscopic surface to the microscopic channels. Such uniform infiltration from the external surface to the inner pore channels not only preserves the integrity of the scaffold architecture, but also significantly enhances the waterproof and antifouling capability of the material under nonplanar structural conditions.

Together with the micro/nanostructured scaffold, the hydrophobic layer gives rise to a typical lotus-leaf-like effect, under which water droplets readily roll off the surface and remove adhered particulates, demonstrating effective self-cleaning behavior (Fig. 3d). The

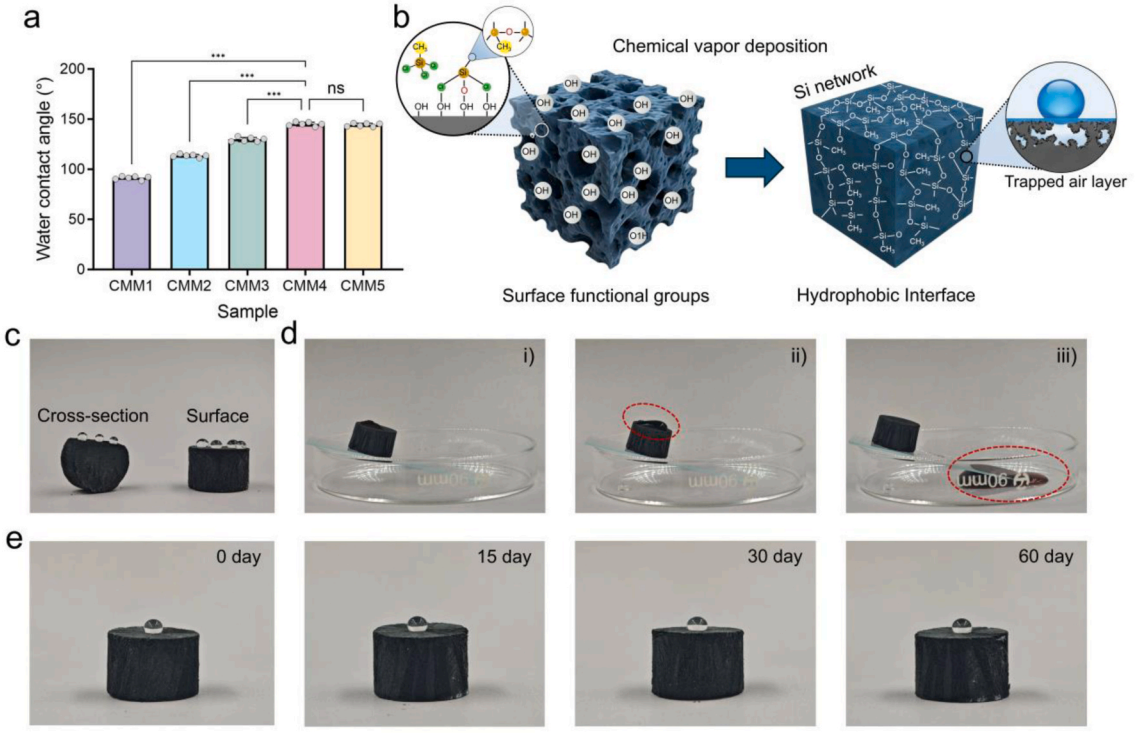

Fig. 3. Hydrophobic performance and aging stability of the CMM_y aerogel. a) Static WCA of CMM_y aerogels as a function of MTS dosage. b) Schematic illustration of the hydrolysis and condensation of MTS on the CM scaffold, forming a Si–*O*–Si-based hydrophobic network. c) Static WCA measured on the outer surface and cross-sectional surface of the CMM_4 aerogel. d) Self-cleaning behavior of the CMM_4 aerogel, where rolling droplets remove dust particles from the surface. e) Variation in the static WCA of the CMM_4 aerogel during 60 days of aging.

environmental durability of the hydrophobic interfacial layer was further evaluated by aging the CMM_4 sample under ambient conditions (25°C, 50% RH). Even after 60 days, the WCA remained above 145° (Fig. 3e), indicating that the Si–*O*–Si/-CH_3 hydrophobic network possesses good chemical stability and structural robustness. This durable interfacial layer effectively suppresses moisture-induced scaffold softening and interfacial slippage, thereby preserving the hydrophobic performance over prolonged storage. In situ MTS vapor-phase deposition establishes a continuous and uniform hydrophobic network from the outer surface to the inner pore channels. Coupled with chemical anchoring and micro/nano-hierarchical roughness, this interfacial regulation imparts strong liquid repellency, self-cleaning capability, and long-term stability to the CMM_4 aerogel, thus highlighting its promise for waterproof and self-cleaning flexible interfaces.

2.4. *Electrical performance evaluation and response mechanism of the flexible pressure sensor*

A flexible piezoresistive pressure sensor was fabricated using the CM_4M aerogel (with a fixed MTS dosage of 1.5 g) as the functional sensing layer. Unless otherwise specified, all aerogels discussed in this section share this fixed MTS dosage and are denoted as CM_xM, where x represents the MXene-to-CNF mass ratio. The device adopts a typical electrode/aerogel/electrode sandwich configuration, in which the highly compressible three-dimensional porous scaffold and uniformly distributed MXene conductive network provide the structural basis for efficient transduction of external pressure into electrical signals (Fig. 4). Fig. 4a further illustrates the microstructural evolution and charge-transport behavior of the CM_xM sensor during compression. The piezoresistive response mainly arises from the combined contributions of quantum tunneling and conformal contact conduction. Comparative electrical analyses (Fig. S7) reveal that while the ultrathin conformal siloxane encapsulation slightly increases the interfacial contact resistance (Fig. S7a) and subsequently causes a minor drop in bulk conductivity (Fig. S7b), it remains thin enough to permit efficient quantum tunneling. Thus, excellent overall conductivity is preserved alongside significantly enhanced environmental stability. In the initial state, adjacent MXene nanosheets remain separated by micro-/nanoscale gaps within the porous framework. Under compression, the reduced inter-sheet distance and increased conductive contacts progressively enhance electron transport, resulting in a pronounced piezoresistive response. This continuous transition from tunneling-assisted transport to direct-contact conduction underlies the high sensitivity and broad sensing range of the CM_xM sensor.

Regulating the MXene loading effectively tunes the density of the internal conductive network in the CM_xM aerogel, thereby enabling tunable electrical performance of the device. The I–V curves show that electrical conductance increases significantly with increasing MXene content (Fig. 4b), indicating good electrical tunability. Based on these I–V curves, the bulk electrical conductivities of the aerogels were calculated to quantitatively evaluate the MXene network's contribution. As the MXene content increases, the electrical conductivity exhibits a significant enhancement, rising from 0.000499 S/m (CM_1M) to 0.021013 S/m (CM_5M) (Table S1, Fig. S8). It is worth noting that while these zero-pressure I–V curves exhibit stable macroscopic Ohmic linearity, the conductivity increase is not strictly proportional to the MXene content. This non-proportionality reflects the inherent interfacial contact resistance between adjacent MXene nanosheets. At lower contents,

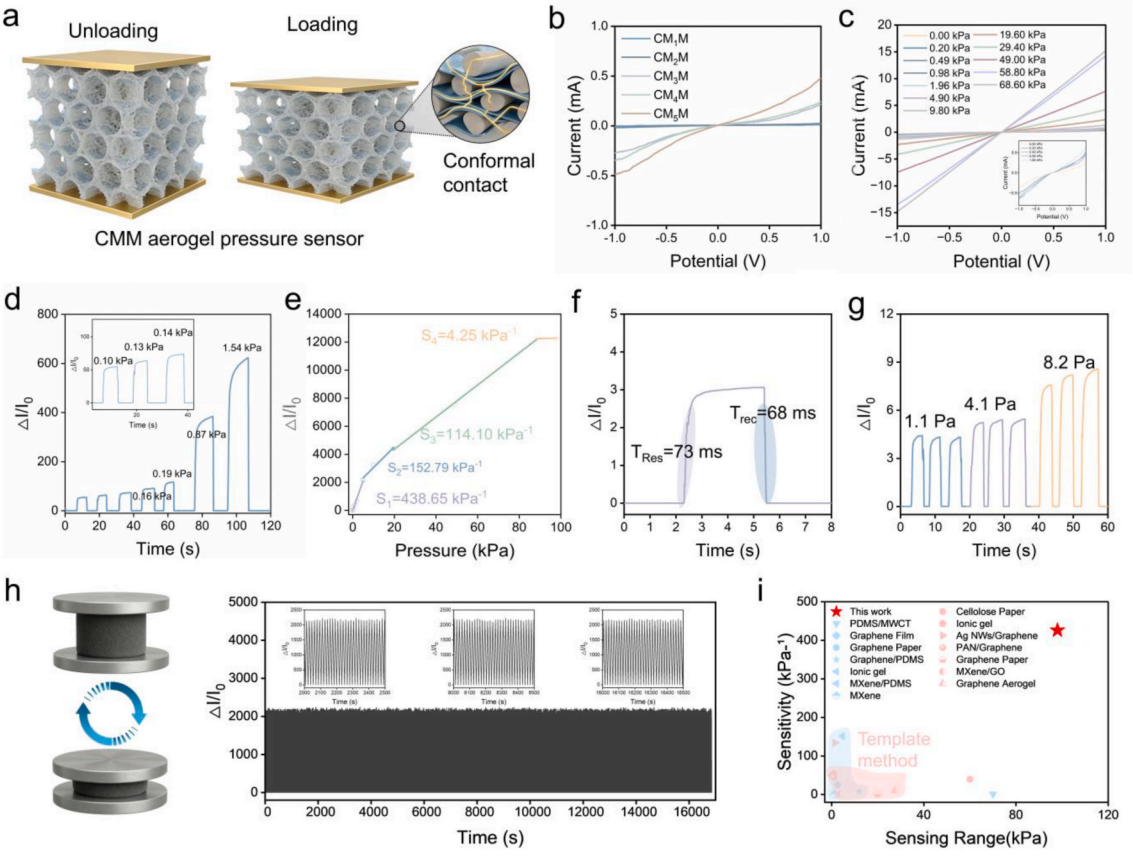

Fig. 4. Electrical and sensing performance of the CMxM aerogel sensor. a) Schematic of the sandwich structure and pressure-induced conduction mechanism. b, c) I–V curves with varying b) MXene loadings and c) applied pressures. d) Relative current response ($\Delta I/I_0$) under varying pressures and e) Sensitivity curve. f) Response and recovery characteristics. g) $\Delta I/I_0$ at ultralow pressures. h) Cycling stability over 1000 cycles at 6.8 kPa. i) Sensitivity and sensing range comparison with other reported sensors.

the inter-sheet gaps and contact resistance dominate, whereas higher MXene loadings facilitate the formation of continuous pathways that effectively overcome these interfacial barriers. Notably, the optimized formulation (CM_4M) achieves a bulk conductivity of 0.010539 S/m. This steady increase confirms the establishment of more effective conductive pathways within the vertically aligned lamellar channels, which is essential for achieving high piezoresistive sensitivity. Under applied pressure, the optimized CM_4M sensor exhibits distinct I–V characteristics at different pressure levels (Fig. 4c), suggesting progressive collapse of the pore units, reduced intersheet distance between MXene nanosheets, and increased effective conductive contact area. The conductance gradually increases with increasing pressure, exhibiting distinct pressure-dependent electrical characteristics. The device is able to stably track real-time variations under different pressure intensities.

As shown in Fig. 4d, the sensor generates clear and distinguishable $\Delta I/I_0$ response signals during loading–unloading cycles under different applied pressures. The signal amplitude increases progressively with pressure, while all cyclic curves exhibit rapid response, good recovery, and small hysteresis, indicating excellent pressure resolution and electromechanical reversibility. As shown in Fig. 4e, the sensor exhibits a distinct piecewise linear response over the pressure range of 0-98 kPa, with sensitivities of 438.65 kPa^{-1} (0-4.9 kPa), 152.79 kPa^{-1} (4.9-19.6 kPa), 114.10 kPa^{-1} (19.6-88.2 kPa), and 4.25 kPa^{-1} (88.2-98 kPa), respectively. This stepwise decrease in sensitivity is highly consistent with the gradual transition of the aerogel scaffold from an initially compressible state to a progressively densified state: in the low-pressure region, slight deformation can significantly modulate the tunneling distance and the number of conductive contact points, whereas in the high-pressure region the remaining adjustable structural space becomes limited, leading to a more moderate response. Specifically, as the lamellar framework undergoes severe progressive densification under higher pressures, the internal free pore volume is nearly exhausted, causing the macroscopic structural deformation to approach a state of saturation. The MXene conductive network transitions into a highly packed configuration dominated by extensive face-to-face mechanical contacts. Once these continuous macroscopic conductive pathways are fully constructed, the creation of new conductive contact points is severely restricted, causing the marginal variation in contact resistance to sharply diminish. This synergistic saturation in both structural compressibility and conductive network reconstruction fundamentally elucidates the stepwise decline in sensitivity in the high-pressure regime.

Further dynamic tests demonstrate that the device possesses rapid force-to-electricity conversion capability, with response and recovery times of 73 and 68 ms, respectively (Fig. 4f). This fast response arises from the rapid deformation capability of the lightweight porous CM_4M scaffold under external stimuli, together with the reversible reconstruction of the MXene conductive network during compression and release. Furthermore, as shown in Fig. 4g, the sensor still delivers clear and distinguishable response signals under ultralow pressure. Even at a pressure of 1.1 Pa, the device maintains a stable $\Delta I/I_0$ change, indicating excellent capability for subtle pressure detection. Long-term cycling tests further show that during 1000 repeated loading–unloading cycles at 6.8 kPa, the sensor output remains highly stable (Fig. 4h). Furthermore, locally enlarged response curves from the initial and final stages of the cycling test reveal that the sensor maintains highly consistent signal waveforms and response amplitudes without any obvious baseline drift, comprehensively confirming its excellent structural stability and antifatigue performance under extended operation. This excellent cycling stability can be attributed to the elastic CNF scaffold and the stable interfacial interactions between MXene nanosheets and the cellulose framework, which together enable reversible conductive-network reconstruction during cyclic deformation. Compared with previously reported flexible pressure sensors (Fig. 4i–Table S2), the CM_4M sensor developed in this work exhibits highly competitive overall performance in terms of sensitivity, sensing range, response speed, and cycling stability, demonstrating the significant advantages of this porous conductive aerogel design for the construction of high-performance flexible piezoresistive sensors [21–33].

2.5. Physiological signal monitoring and expanded Human–Machine interaction applications

Benefiting from the hierarchical porous architecture, compressible scaffold, and stable conductive network of the optimized CMM aerogel (defined as the optimal CM4M4 formulation, CNF:MXene mass ratio of 2:4 with a fixed MTS dosage of 1.5 g), the resulting piezoresistive sensor exhibits excellent mechanical compliance and reliable electrical output. This enables the robust detection of human motion, physiological signals, and human–machine interaction inputs. Owing to its thin and compliant structure, the device can conformally attach to irregular body surfaces, which helps reduce motion artifacts and improves wearing comfort during prolonged use (Fig. 5a). When attached to the finger, the sensor clearly distinguishes different types of mechanical stimuli, including light touch and firm touch. Finger touch generates sharp and rapid current signals (Fig. 5b), indicating a prompt response to different dynamic pressure inputs. By contrast, finger bending produces stable low-frequency periodic signals (Fig. 5c), reflecting the capability of the device to monitor continuous and slowly varying mechanical deformation. These results confirm its suitability for motion sensing and basic behavioral recognition. When mounted on joints, the sensor can track deformation-induced pressure changes in real time. Stable and reproducible signals are obtained under wrist bending (Fig. 5d), demonstrating good flexibility, conformability, and mechanical durability. In addition, when integrated into the back-contact region, the device differentiates sitting postures according to changes in pressure distribution between the body and the chair surface (Fig. 5e), suggesting potential utility in posture monitoring and sedentary-behavior management.

For physiological monitoring, the sensor was conformally attached above the radial artery and enabled stable acquisition of pulse-related mechanical signals. As compared in Fig. 5f, the pulse waveform remains regular before the 100 m run (76 bpm), whereas the signal frequency noticeably increases to 114 bpm after the 100 m run. To further verify the validity and resolution of the physiological signals, a single pulse waveform was magnified and analyzed (Fig. 5g). The sensor accurately captures the typical characteristic peaks of a standard human radial artery pulse, including the incident wave (P wave), the tidal wave (T wave), and the dicrotic wave (D wave). The clear distinguishability of these minute physiological features demonstrate that the device can sensitively track pulse variations under different physiological states, supporting its use in daily health monitoring and exercise-state assessment. The sensor also responds sensitively to airflow disturbance. A slight blowing stimulus triggers a pronounced current change (Fig. 5h), indicating potential for airflow sensing and respiration-related monitoring. In addition, when attached to the throat, the device records in real time the local pressure fluctuations induced by vocal-cord vibration during phonation (Fig. 5i). The pronunciation of “Ni Hao” yields a clearly recognizable signal pattern. This behavior supports the feasibility of the sensor for wearable speech-related signal recognition and interactive input. Its applicability in human–machine communication was further examined through a simulated Morse-code input test (Fig. 5j). Short presses (“·”) and long presses (“–”) corresponding to the “SOS” and “YES” sequences were stably distinguished and correctly decoded, demonstrating the capability of the device to convert mechanical input into recognizable interaction commands.

Notably, the device maintains good operational stability even under high-humidity conditions. Fig. 5k compares the response behaviors of CMM and unmodified CM sensors after 7 days of exposure to 93% RH. Under this high-humidity condition, the CMM sensor still retains clear and stable electrical signal output, whereas the response of the CM sensor shows obvious attenuation. Specifically, as suggested by the structural and chemical evolution of the unmodified CM sensor, this

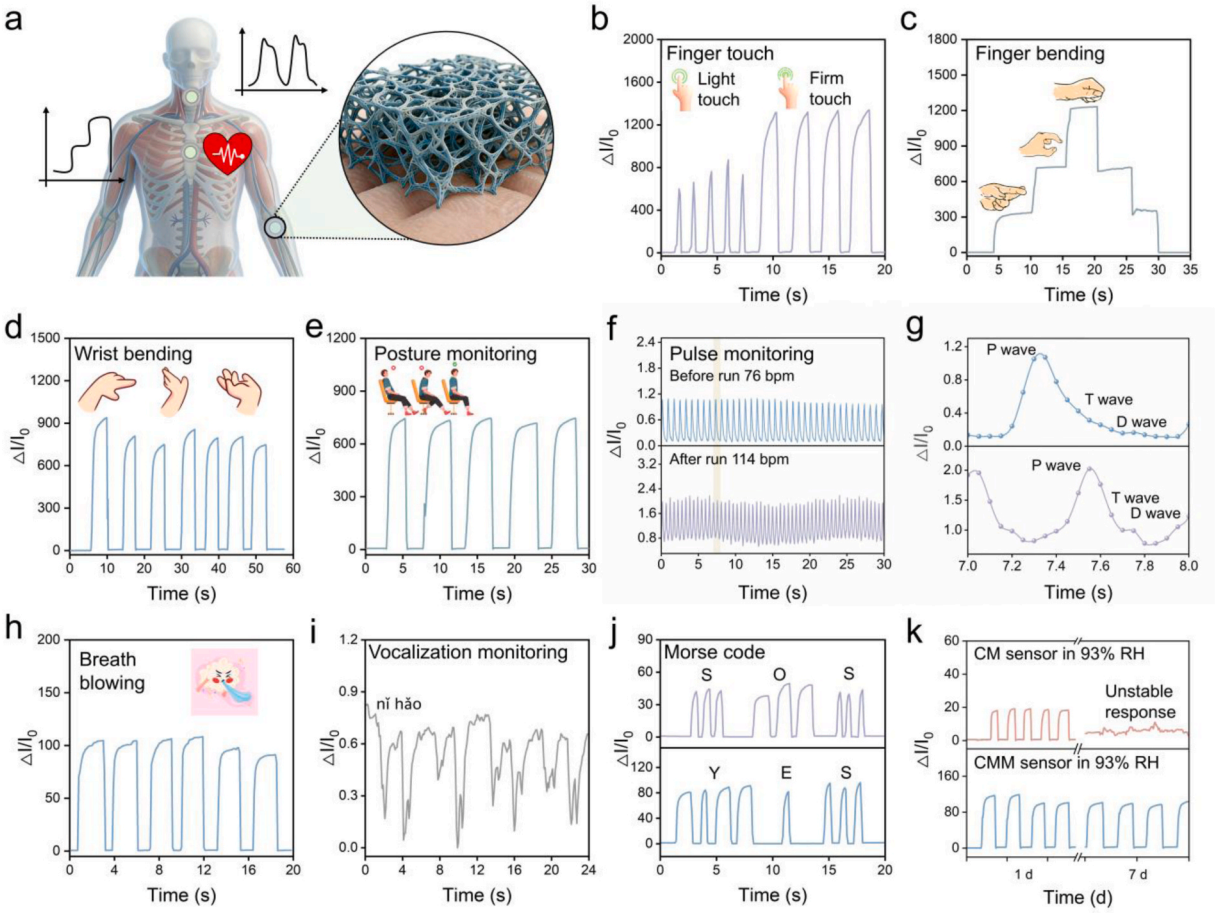

Fig. 5. Multimodal physiological monitoring and human–machine interaction using the CMM aerogel sensor. a) Schematic of the sensor on the human body and its porous structure. b-e) Δ I/I_0 to b) light/firm touch, c) finger bending, d) wrist bending, and e) posture changes. f) Pulse signals before and after a 100 m run. g) Magnified single pulse waveform showing P, T, and D waves. h) Response to breath blowing. i) Vocalization signals of "nǐ hǎo". j) Morse-code input ("SOS", "YES"). k) Stability comparison between CM and CMM sensors at 93% RH.

severe signal drift under high humidity is driven by a dual degradation mechanism. On one hand, the adsorption of water molecules plasticizes the hydrophilic CNF framework, leading to structural softening. On the other hand, the permeated moisture triggers the rapid oxidation of highly active MXene nanosheets into insulating TiO_2, as confirmed by the emergence of TiO_2 peaks in the XRD pattern (Fig. S9) and the significant enhancement of Ti–O bonds in the XPS spectra (Figs. S10–S11) after aging. This chemical degradation substantially decreases the intrinsic conductivity of the interconnected MXene network. By contrast, the robust siloxane (Si–O–Si) hydrophobic layer constructed via MTS vapor-phase deposition functions as an effective physical barrier. It impedes moisture penetration, thereby simultaneously preserving the structural rigidity of the porous framework and shielding the MXene conductive network from environmental oxidation. To further evaluate long-term reliability, the electrical baseline stability of CM and CMM aerogels was monitored at 97 ± 2% RH for 20 days (Fig. S12). Moisture-induced MXene oxidation and structural degradation caused a severe baseline current decay in the unmodified CM sensor. Furthermore, after 20-day aging, the CM sensor exhibited severely diminished piezoresistive sensitivity and distorted signal outputs (Fig. S13). In sharp contrast, the MTS-modified CMM sensor maintained a highly stable baseline current and perfectly preserved its high sensitivity across the entire pressure range. These results collectively demonstrate that the hydrophobic siloxane interface effectively protects the internal conductive framework from moisture, ensuring long-term sensing reproducibility. The flexible piezoresistive sensor based on the CMM aerogel enables effective recognition of multiple types of mechanical signals, including human motion, pulse, airflow, and speech, while maintaining stable output in humid environments. These results demonstrate the strong application potential of this material system in human–machine interaction, health monitoring, and complex-environment sensing.

2.6. Photothermal conversion and thermal-management performance

Benefiting from the excellent electron-transport capability of MXene and the three-dimensional continuous conductive network constructed within the aerogel scaffold, the CM_xM_4 aerogel series exhibits efficient energy conversion behavior (Fig. 6a). In this architecture, directionally assembled MXene nanosheets form continuous electron-transport pathways along the scaffold, while the lamellar porous framework provides low-resistance channels for heat diffusion. This synergistic coupling of electron transport and thermal diffusion enables externally input energy to be rapidly converted and uniformly released on the macroscopic scale, achieving a rapid and stable thermal response even under relatively low energy input. Under irradiation intensities of 109, 211, and 314 mW cm^{-2}, the aerogel rapidly reaches stable thermal plateaus of 80.1, 109.6, and 179.6°C within 89 s, respectively (Fig. 6b). Notably, under 314 mW cm^{-2} irradiation, the maximum temperature of the CM_4M_4 sample (179.6°C) is significantly higher than that of the unmodified sample (136.7°C, Fig. S14). The CM_4M_4 formulation is hereafter denoted as CMM. This enhancement confirms that the conformal siloxane interfacial regulation, together with the ordered heat-conduction network, effectively boosts photothermal efficiency.

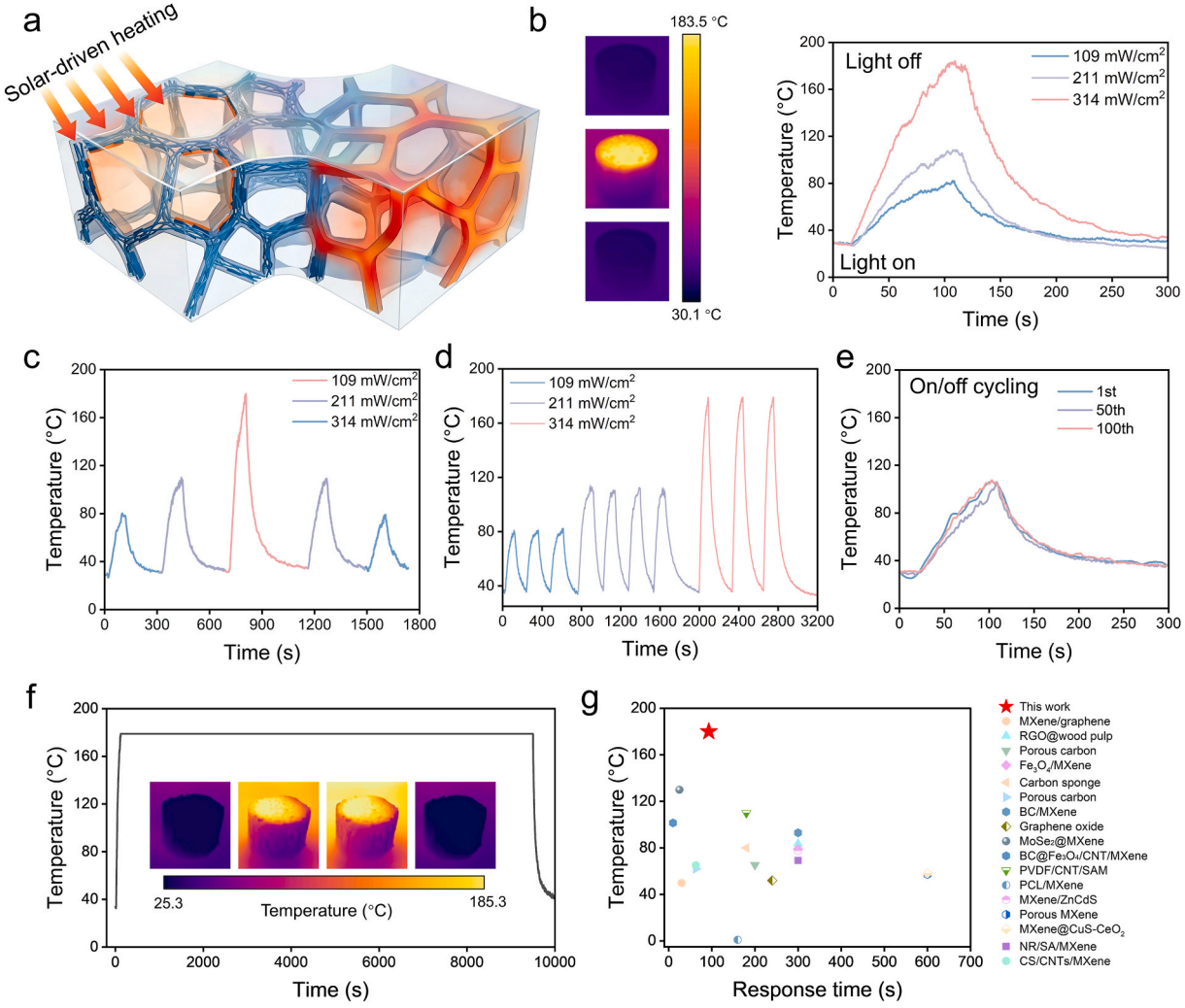

Fig. 6. Photothermal performance and thermal stability of the CM_xM_4 composite aerogel. a) Schematic illustration of the photothermal conversion and heat-transfer behaviour of the aerogel. b) Infrared thermal images and corresponding temperature evolution of the CM_xM_4 aerogel under different irradiation intensities. c) Reversible surface temperature response of the aerogel under stepwise irradiation intensities. d) Photothermal heating–cooling curves of the aerogel over three on/off cycles under different irradiation intensities. e) Comparison of the temperature-rise curves in the 1st, 50th and 100th cycles, demonstrating stable photothermal cycling performance. f) Continuous photothermal heating behaviour under an irradiation intensity of 314m W cm^{-2}, showing stable thermal output over more than 9563 s. g) Comparison of the photothermal performance of the present aerogel with previously reported materials.

This enhancement arises from two synergistic effects: the broadband visible-to-near-infrared absorption of MXene for efficient light harvesting, and the multiscale roughness of the conformal siloxane encapsulation, which promotes multiple light scattering and localized absorption within the pore channels. The corresponding infrared thermal images further reveal a relatively uniform surface temperature distribution, with a temperature difference of only about 3°C between the center and edge regions at the thermal plateau, indicating that the constructed three-dimensional framework can effectively suppress local heat accumulation and enable homogeneous heat release.

Furthermore, the thermal response of the sample is strongly influenced by both the MXene content and MTS interfacial regulation (Fig. S15). Under a fixed irradiation intensity, the maximum temperature increases from 91°C to 179.6°C with increasing MXene content, indicating that the gradual improvement of the conductive network and electron-transport efficiency enhances both the photothermal conversion capability. However, when the MXene content is further increased to a mass ratio of 2:5, the maximum temperature decreases to 159.6°C. This decline is mainly attributed to excessive restacking of MXene nanosheets, which restricts the internal pore structure and weakens multiple light scattering and absorption within the porous framework, while also being unfavorable for structural elasticity and interfacial stability. As a result, the photothermal/electrothermal performance as a function of composition exhibits a typical volcano-like trend, reflecting the synergistic coupling among conductive-network formation, interfacial regulation, and porous-structure optimization.

Beyond steady-state performance, the aerogel demonstrates excellent dynamic thermal responsiveness and reversibility. The surface temperature exhibits a rapid and reversible response to stepwise changes in irradiation intensity, closely tracking the applied optical stimuli with no hysteresis (Fig. 6c). This highly reversible behavior extends to cyclic operations (Fig. 6d). As the irradiation intensity increases, the peak cycling temperatures remain stable at approximately 80.1, 109.6, and 179.6°C, respectively, with no obvious thermal attenuation observed during repeated light on/off cycles. At the same time, the sample cools rapidly and returns close to the initial temperature after the light source is removed, further confirming the good reversibility of the thermal response process. Furthermore, the nearly overlapping temperature-rise curves for the 1st, 50th, and 100th cycles (109.6°C) confirm its exceptional long-term photothermal cycling stability (Fig. 6e). This stable cycling behaviour suggests that the CMM aerogel can maintain efficient light-to-heat conversion and structural integrity

under prolonged cyclic irradiation.

To evaluate its limits under continuous energy input, the CMM composite aerogel was rapidly heated to approximately 170-180°C under continuous light irradiation and maintained a stable thermal output plateau for as long as 9563 s, without obvious temperature decay (Fig. 6f). This result demonstrates the excellent sustainability and structural stability of its photothermal conversion process. It also indicates that the continuous heat-conduction network constructed within the material can maintain efficient heat transfer and uniform heat release under prolonged energy input, thereby endowing the aerogel with good long-term thermal-management capability. The MXene conductive network, lamellar porous scaffold, and conformal siloxane layer together establish a multiscale synergistic mechanism of light absorption–electron transport–thermal conversion–thermal diffusion (Fig. 6g). Compared with previously reported materials, the present CMM composite aerogel exhibits significant advantages in temperature-rise efficiency, response speed, and cycling stability, highlighting its broad application prospects in flexible heaters, intelligent wearable thermal-management systems, and thermal regulation under complex environmental conditions [34–51].

To elucidate the bidirectional force–thermal coupling of the CMM aerogel, we further investigated its multi-field performance. First, the sensor maintained highly stable pressure sensitivity with no thermal degradation under varying environmental heating temperatures (Fig. S16). Furthermore, continuous light irradiation (54, 89, and 131m W cm^{-2}) did not compromise its sensing reliability or linear ranges (Fig. S17). Conversely, the reciprocal photothermal behavior under mechanical deformation showed that the aerogel retained highly efficient and stable temperature-time evolution profiles even under varying compressive strain states (Fig. S18). These results indicate that the progressive densification of the CNF/MXene framework preserves intact light scattering channels and robust thermal conduction pathways.These findings demonstrate that the structural–interfacial synergistic design endows the aerogel with exceptional dual-mode reliability, ensuring stable operation in complex, multi-field coupled environments.

3. Discussions

This work addresses a central challenge of porous conductive aerogels for operation in complex environments, namely the difficulty of simultaneously achieving high sensitivity and long-term stability. To this end, a synergistic strategy of structural ordering and interfacial stabilization was proposed to construct a CMM composite aerogel featuring vertically aligned lamellar channels and a hydrophobic interface. The results demonstrate that the ordered pore architecture generated by directional freezing can effectively constrain the compressive deformation pathway and guide MXene nanosheets to form a continuous yet confined conductive network along the pore walls. Meanwhile, the stable hydrophobic interface formed by in situ MTS vapor-phase deposition significantly suppresses humidity-induced scaffold softening, interfacial slippage, and conductive instability. Owing to the synergy between structural regulation and interfacial regulation, the material achieves a transition from a “random structure–random response” mode to an “ordered structure–controllable response” mode. As a result, the obtained aerogel exhibits a highly sensitive piezoresistive response over 0-98 kPa, with a maximum sensitivity of 438.65 kPa^{-1}, while maintaining good signal stability after more than 10,000 loading–unloading cycles. In addition, the material shows excellent environmental adaptability and thermal-management capability, reaching a maximum temperature of 179.6°C under light irradiation. More importantly, this study reveals a key principle governing the reliability of porous conductive aerogels, namely that device reliability is jointly determined by the controllability of the deformation pathway and the stability of the interfacial environment. These findings provide a new physical picture and a general design strategy for the development of highly reliable flexible sensors and intelligent thermal-management materials for extreme environments.

4. Experimental section

4.1. Materials

Titanium aluminum carbide (Ti_3AlC_2) was purchased from Sinopharm Chemical Reagent Co., Ltd. Conductive silver paste was obtained from Zhuhai Kejin Technology Co., Ltd. Hydrochloric acid (HCl), lithium fluoride (LiF), and methyltrichlorosilane (CH_3SiCl_3, MTS) were supplied by Shanghai Aladdin Biochemical Technology Co., Ltd. Bleached softwood dissolving pulp was supplied by Shandong Sun Paper Industry Co., Ltd.

4.2. Preparation of CNFs

Bleached softwood pulp was dispersed in deionized water (DI) to prepare a uniform slurry with a solid content of 10 wt%. The slurry was then refined in a PFI mill at 3.33 N mm^{-1} for 80,000 revolutions to obtain mechanically fibrillated cellulose pulp. The refined pulp was subsequently passed through a high-pressure homogenizer at 1000 bar for eight passes to yield a uniform cellulose nanofiber (CNF) suspension. The concentration of the final suspension was adjusted to 1.31 wt%, and the suspension was stored at 4°C before use.

4.3. Preparation of MXene

MXene was prepared by selective etching of Ti_3AlC_2 according to a previously reported method [7]. Briefly, 1.6 g of LiF was dissolved in 20 mL of 9 M HCl in a polytetrafluoroethylene (PTFE) flask under magnetic stirring for 30 min at room temperature. Subsequently, 1 g of Ti_3AlC_2 powder (MAX phase) was slowly added to the solution, and the mixture was stirred at 40°C for 48 h for etching. Afterward, the reaction product was repeatedly washed with deionized water until the pH of the supernatant reached approximately 7. The resulting sediment was then redispersed in 35 mL of ice-cold deionized water and sonicated for 1 h, followed by centrifugation at 3500 rpm for 1 h. The supernatant was collected as the MXene nanosheet dispersion, and its concentration was determined by a gravimetric method.

4.4. Fabrication of CNF/MXene aerogels with directional pore architecture and hydrophobic interface

Freeze-dried MXene powder was added to a prepared CNF aqueous dispersion (1.31 wt%) and ultrasonicated for 30 min to form a stable and homogeneous CNF/MXene suspension. The suspension was then drop-cast onto a copper plate precooled to liquid-nitrogen temperature. Under the steep temperature gradient, ice crystals grew directionally along the vertical direction during a 12 h freezing process. The resulting frozen monolith was subsequently freeze-dried at −50°C for 48 h to obtain CNF/MXene aerogels with highly ordered channel structures. The dried aerogels were placed in a sealed container and exposed to different amounts of MTS (0.2, 0.5, 1.0, 1.5, and 2.0 g) for vapor-phase deposition at room temperature for 2 h. MTS reacted with the hydroxyl groups on the CNF surface to form a hydrophobic organosilane layer, thereby imparting excellent hydrophobicity and structural stability to the aerogels. Composite aerogels with different compositions were prepared by varying the mass ratio of CNF to MXene (2:1, 2:2, 2:3, 2:4, and 2:5), and the samples were denoted as CM_x, where x represents the mass ratio of MXene relative to CNF. According to the MTS dosage, the modified samples were further denoted as CM_xM_y, where y represents the MTS dosage group ($y = 1$-5, corresponding to 0.2, 0.5, 1.0, 1.5, and 2.0 g of MTS, respectively).

4.5. Fabrication of flexible pressure sensors

Flexible pressure sensors were fabricated by sandwiching the active aerogel layer between two parallel copper-foil electrodes. The copper foils served as the positive and negative electrodes and were firmly bonded to the active layer using conductive silver paste to ensure reliable electrical contact.

4.6. Characterization and testing

The microstructure and morphology of the samples were characterized by field-emission scanning electron microscopy (FE-SEM, Merlin, Zeiss, Germany), atomic force microscopy (AFM, MultiMode 8, Bruker, USA), and transmission electron microscopy (TEM, JEM-2100F, JEOL, Japan). Energy-dispersive X-ray spectroscopy (EDS, Oxford, UK) coupled with FE-SEM was used to analyze the elemental distribution and spatial arrangement of the CNF/MXene aerogels. The interfacial chemical composition and bonding characteristics were analyzed by Fourier-transform infrared spectroscopy (FTIR, Nexus 470, Thermo Nicolet, USA) and X-ray photoelectron spectroscopy (XPS, Axis Supra+, Kratos, UK). The crystal structure and crystallinity of the aerogels were characterized by X-ray diffraction (XRD, X'Pert^3, PANalytical B.V., Netherlands) over a 2θ range of 2–50° at a scan rate of 5° min^{-1}. The hydrophobicity of the samples was evaluated using a contact-angle goniometer (ZJ-7000, Zhijia, China). During testing, a 10 μL droplet of deionized water was placed on the sample surface, and the static contact angle was recorded. The electromechanical response of the flexible pressure sensors was evaluated by applying cyclic loading using a universal testing machine (Instron 5565, USA), while the resistance change was monitored in real time using an electrochemical workstation (CHI660E, China) at an applied voltage of 1 V. The bulk electrical conductivity (σ) of the composite aerogels was calculated from the resistance (R) obtained from the linear region of the current-voltage curves, using the following equation: $\sigma = L/(R \times A)$, where L and A represent the thickness and the cross-sectional area of the sample, respectively. For photothermal measurements, the aerogel samples were irradiated with a xenon lamp simulating solar illumination, and the temperature evolution was recorded using an infrared thermal camera (FOTRIC 325C, China). Different light intensities were achieved by adjusting the distance between the light source and the sample, while the irradiance was monitored in real time using a solar power meter (TM-207, Tenmars, Taiwan).

CRediT authorship contribution statement

Ao Li: Conceptualization, Data curation, Investigation, Methodology, Writing – original draft. **Jun Xu:** Conceptualization, Funding acquisition, Project administration, Supervision, Writing – review & editing. **Dezhong Xu:** Data curation, Formal analysis, Writing – original draft. **Zhaohui Zhang:** Validation. **Shengtao Zhou:** Resources. **Hanyuan Chen:** Conceptualization. **Kefu Chen:** Visualization. **Mizi Fan:** Supervision, Writing – review & editing.

Declaration of competing interest

The authors declare no competing financial interest.

Acknowledgements

This work was supported by the Guangdong Key R&D Program (2022B111108004), the Taishan Industrial Experts Programme (TSCX202211068), the Fundamental Research Funds for the Central Universities (2025ZYGXZR004, D2250060), the Research Funds of SKLAPPM (2024ZD07, 2025PT03), and the European Innovation Council Pathfinder (HORIZON-EIC-2023-PATHFINDEROPEN-01 (No.101130895)).

Appendix A. Supplementary data

Supplementary data to this article can be found online at https://doi.org/10.1016/j.compositesb.2026.113877.

Data availability

Data will be made available on request.

References

[1] Li Y, Wang Y, Wang X, Wang Y, Zhang B, Li R, et al. Linear range enhancement in flexible piezoresistive sensors enabled by double-layer corrugated structure. Adv Funct Mater n.d.;n/a:e13480. https://doi.org/10.1002/adfm.202513480.
[2] Zhu R, Kang L, Yao R, Wu J, Zhang J. Textile-derived stiffness-gradient piezoresistive elastomeric composites for modulus-programmable wearable sensors. Compos B Eng 2026;314:113450. https://doi.org/10.1016/j.compositesb.2026.113450.
[3] Tan Z, Hu Q, Yang B, Liu W, Zhang Z, Shu L, et al. Superelastic and highly sensitive biomass-derived piezoresistive aerogels for deep-learning-assisted sensing. Adv Funct Mater n.d.;35:e11831. https://doi.org/10.1002/adfm.202511831.
[4] Yang M, Wang Y, Li M, Wang B, Sun S, Wan C, et al. Self-powered flexible piezo-photoelectric dual-mode sensor based on PVDF-TrFE combined with MXene@TiO2 heterojunction. Compos B Eng 2026;310:113161. https://doi.org/10.1016/j.compositesb.2025.113161.
[5] Li L, Cheng Y, Cao H, Liang Z, Liu Z, Yan S, et al. MXene/rGO/PS spheres multiple physical networks as high-performance pressure sensorMXene/rGO/PS. Nano Energy 2022;95:106986. https://doi.org/10.1016/j.nanoen.2022.106986.
[6] Li A, Xu J, Xu D, Zhang Z, Deng Z, Cao D, et al. Multilayered cellulose nanofiber/MXene-based dual-mode sensor for monitoring sleep quality and respiratory disorders. Chem Eng J 2025;514:163426. https://doi.org/10.1016/j.cej.2025.163426.
[7] Li A, Xu J, Xu D, Zhang Z, Cao D, Li J, et al. High-performance, breathable, and degradable fully cellulose-based sensor for multifunctional human activity monitoring. Chem Eng J 2025;505:159564. https://doi.org/10.1016/j.cej.2025.159564.
[8] Qin D, Liu C, Song K, Ramakrishna S. Bioinspired silk fibroin/poly-acrylic acid high-performance hydrogel sensors with micro-architecture prepared by rapid polymerization via TA-Fe3O4@MXene catalytic system. Chem Eng J 2025;525:170300. https://doi.org/10.1016/j.cej.2025.170300.
[9] Liu L, Sun Y, Luo H, Ao Y, Jin L. Boosting EMI Shielding and Joule Heating in Carbon Fiber Paper through lotus seedpod-inspired core-shell nickel nanospheres/MXene hierarchical reinforcement layer. Compos B Eng 2026;313:113411. https://doi.org/10.1016/j.compositesb.2026.113411.
[10] Ren J, Huang X, Han R, Chen G, Li Q, Zhou Z. Avian bone-inspired super fatigue resistant MXene-Based aerogels with human-like tactile perception for multilevel information encryption assisted by machine learning. Adv Funct Mater 2024;34:2403091. https://doi.org/10.1002/adfm.202403091.
[11] Xu T, Song Q, Liu K, Liu H, Pan J, Liu W, et al. Nanocellulose-Assisted construction of multifunctional MXene-Based aerogels with engineering biomimetic texture for pressure sensor and compressible electrode. Nano-Micro Lett 2023;15:98. https://doi.org/10.1007/s40820-023-01073-x.
[12] Li A, Xu J, Zhou S, Zhang Z, Cao D, Wang B, et al. All-Paper-Based, flexible, and bio-degradable pressure sensor with high moisture tolerance and breathability through conformally surface coating. Adv Funct Mater n.d.;34:2410762. https://doi.org/10.1002/adfm.202410762.
[13] Lee D, Choi J. Freeze-casted aerogel-based piezoresistive pressure sensors: materials, structures, and applications. Micro and Nano Syst Lett 2025;13:21. https://doi.org/10.1186/s40486-025-00242-4.
[14] Oh J, Kim J-O, Kim Y, Choi HB, Yang JC, Lee S, et al. Highly uniform and low hysteresis piezoresistive pressure sensors based on chemical grafting of polypyrrole on elastomer template with uniform pore size. Small 2019;15:e1901744. https://doi.org/10.1002/smll.201901744.
[15] Min P, Li X, Liu P, Liu J, Jia X-Q, Li X-P, et al. Rational design of soft yet elastic lamellar graphene aerogels via bidirectional freezing for ultrasensitive pressure and bending sensors. Adv Funct Mater 2021;31:2103703. https://doi.org/10.1002/adfm.202103703.
[16] Gao Y-C, Yu Z-L, Qin B, Chen C, Ma Z-Y, Yu S-H. Superflexible artificial soft wood. Adv Mater 2023;35:2303518. https://doi.org/10.1002/adma.202303518.
[17] Liu J, Zhang X, Liu J, Liu X, Zhang C. 3D printing of anisotropic piezoresistive pressure sensors for directional force perception. Adv Sci 2024;11:2309607. https://doi.org/10.1002/advs.202309607.
[18] Long X, Qin J, Zhou L, Li L, Wang Y, Tang J, et al. Double-negative-index ceramic aerogels featuring a multiscale structural design for thermal superinsulation at extreme conditions. Mater Today 2026;96:103302. https://doi.org/10.1016/j.mattod.2026.103302.
[19] Long X, Qin J, Tang J, Xue J, Wang Y, Zhou L, et al. Hierarchical design of 1D building blocks for anisotropic aerogel. Adv Funct Mater 2025;35:2413018. https://doi.org/10.1002/adfm.202413018.
[20] Long X, Tang J, Luo C, Qin J, Wang Y, Zhou L, et al. Hierarchical building blocks with alternating hard cores and flexible chains for ultrahigh strength aerogel. Nano Lett 2025;25:10303–9. https://doi.org/10.1021/acs.nanolett.5c01080.

[21] Li A, Xu J, Zhou S, Zhang Z, Cao D, Wang B, et al. All-Paper-Based, flexible, and bio-degradable pressure sensor with high moisture tolerance and breathability through conformally surface coating. Adv Funct Mater 2024;34:2410762. https://doi.org/10.1002/adfm.202410762.
[22] Xie H, Huang Z, Wan J, Zhou R, Chen T, Wang Y, et al. Dual-Band Laser selective etching for stretchable and strain interference-free pressure sensor arrays. Adv Funct Mater 2024;34:2401532. https://doi.org/10.1002/adfm.202401532.
[23] Jung Y, Choi J, Lee W, Ko JS, Park I, Cho H. Irregular microdome structure-based sensitive pressure sensor using internal popping of microspheres. Adv Funct Mater 2022;32:2201147. https://doi.org/10.1002/adfm.202201147.
[24] Ge G, Zhang Y, Shao J, Wang W, Si W, Huang W, et al. Stretchable, transparent, and self-patterned Hydrogel-Based pressure sensor for human motions detection. Adv Funct Mater 2018;28:1802576. https://doi.org/10.1002/adfm.201802576.
[25] Li X, Fan YJ, Li HY, Cao JW, Xiao YC, Wang Y, et al. Ultracomfortable hierarchical nanonetwork for highly sensitive pressure sensor. ACS Nano 2020;14:9605–12. https://doi.org/10.1021/acsnano.9b10230.
[26] Pang Y, Zhang K, Yang Z, Jiang S, Ju Z, Li Y, et al. Epidermis microstructure inspired graphene pressure sensor with random distributed spinosum for high sensitivity and large linearity. ACS Nano 2018;12:2346–54. https://doi.org/10.1021/acsnano.7b07613.
[27] Bae GY, Pak SW, Kim D, Lee G, Kim DH, Chung Y, et al. Linearly and highly pressure-sensitive electronic skin based on a bioinspired hierarchical structural array. Adv Mater 2016;28:5300–6. https://doi.org/10.1002/adma.201600408.
[28] Qiu Z, Wan Y, Zhou W, Yang J, Yang J, Huang J, et al. Ionic skin with biomimetic dielectric layer templated from calathea zebrine leaf. Adv Funct Mater 2018;28:1802343. https://doi.org/10.1002/adfm.201802343.
[29] Ren H, Zheng L, Wang G, Gao X, Tan Z, Shan J, et al. Transfer-Medium-Free nanofiber-reinforced graphene film and applications in wearable transparent pressure sensors. ACS Nano 2019;13:5541–8. https://doi.org/10.1021/acsnano.9b00395.
[30] Cheng Y, Ma Y, Li L, Zhu M, Yue Y, Liu W, et al. Bioinspired microspines for a high-performance spray Ti3C2Tx MXene-Based piezoresistive sensor. ACS Nano 2020;14:2145–55. https://doi.org/10.1021/acsnano.9b08952.
[31] Tao L-Q, Zhang K-N, Tian H, Liu Y, Wang D-Y, Chen Y-Q, et al. Graphene-Paper pressure sensor for detecting human motions. ACS Nano 2017;11:8790–5. https://doi.org/10.1021/acsnano.7b02826.
[32] Ma Y, Yue Y, Zhang H, Cheng F, Zhao W, Rao J, et al. 3D synergistical MXene/Reduced graphene oxide aerogel for a piezoresistive sensor. ACS Nano 2018;12:3209–16. https://doi.org/10.1021/acsnano.7b06909.
[33] Zeng Z, Wu N, Yang W, Xu H, Liao Y, Li C, et al. Sustainable-Macromolecule-Assisted preparation of cross-linked, ultralight, flexible Graphene Aerogel sensors toward low-frequency Strain/Pressure to high-frequency vibration sensing. Small 2022;18:2202047. https://doi.org/10.1002/smll.202202047.
[34] Cai Z, Ma Y, Yun M, Wang M, Tong Z, Suhr J, et al. Multifunctional MXene/holey graphene films for electromagnetic interference shielding, Joule heating, and photothermal conversion. Compos B Eng 2023;251:110477. https://doi.org/10.1016/j.compositesb.2022.110477.
[35] Du M, Shi H, Yin R, Yang J, Shi F, Zheng Q, et al. TDA/rGO@WS with Joule heat and photothermal synergistic effect: a promising adsorption material for all–weather recovery of viscous oil spills at sea. J Hazard Mater 2024;466:133542. https://doi.org/10.1016/j.jhazmat.2024.133542.
[36] Song C, Jin Y, Gu X, Shi J. A solar-driven self-repairing sponge for efficient recovery of crude oil. Colloids Surf A Physicochem Eng Asp 2023;658:130692. https://doi.org/10.1016/j.colsurfa.2022.130692.
[37] Wang X, Liu X, Liu Z, Cui W, Gao S, Zhang J, et al. Superhydrophobic aerogel blanket with magnetic and solar heating effect enables efficient continuous cleanup of highly viscous crude oil. J Hazard Mater 2023;445:130594. https://doi.org/10.1016/j.jhazmat.2022.130594.
[38] Wu M-B, Huang S, Liu T-Y, Wu J, Agarwal S, Greiner A, et al. Compressible carbon sponges from delignified wood for fast cleanup and enhanced recovery of crude oil spills by Joule Heat and photothermal effect. Adv Funct Mater 2021;31:2006806. https://doi.org/10.1002/adfm.202006806.
[39] Zeng G, Huang X, Yue J, Fan B, Liu Y, Tang X-Z. Solar-assisted efficient cleanup of high-viscosity oil spills using magnetic porous biochar. J Alloys Compd 2022;924:166474. https://doi.org/10.1016/j.jallcom.2022.166474.
[40] Chen Z, Wang B, Qi J, Liu T, Feng Y, Liu C, et al. Eco-friendly bacterial cellulose/MXene aerogel with excellent photothermal and electrothermal conversion capabilities for efficient separation of crude oil/seawater mixture. Carbohydr Polym 2024;336:122140. https://doi.org/10.1016/j.carbpol.2024.122140.
[41] Chen Z, Su X, Wu W, Zhou J, Wu T, Wu Y, et al. Superhydrophobic PDMS@GSH wood with Joule heat and photothermal effect for viscous crude oil removal. Carbon 2023;201:577–86. https://doi.org/10.1016/j.carbon.2022.09.014.
[42] Xie J, Zhang Y, Dai J, Xie Z, Xue J, Dai K, et al. Multifunctional MoSe2@MXene heterostructure-decorated cellulose fabric for wearable thermal therapy. Small 2023;19:2205853. https://doi.org/10.1002/smll.202205853.
[43] Yang Y, Shao L, Wang J, Ji Z, Zhang T, Wu M, et al. An asymmetric layer structure enables robust multifunctional wearable bacterial cellulose composite film with excellent Electrothermal/Photothermal and EMI shielding performance. Small 2024;20:2308514. https://doi.org/10.1002/smll.202308514.
[44] Dong C, Lin W, Li Z, Chen L, Tang Z, Lu F, et al. Ultra-High freshwater production via coupling Photo-/Electro-Thermal self-heating and self-insulating janus membrane. Adv Funct Mater 2025;35:2423610. https://doi.org/10.1002/adfm.202423610.
[45] Zhang J, Cheng H, Jiao Y, Ye Y, Wang Y, Abd-El-Aziz AS, et al. Photothermal driven shape memory polymer based on MXene-grafted-polycaprolactone with fast response and easy recyclability. Polymer 2026;345:129554. https://doi.org/10.1016/j.polymer.2026.129554.
[46] Lu S, Liu Y, Cao S, Wang S, Tang Z, Wu G, et al. *In-situ* prepared Ti3C2 MXene/Zn0.6Cd0.4S for synergistic photothermal-photocatalytic hydrogen evolution under near-infrared light. Int J Hydrogen Energy 2026;227:154563. https://doi.org/10.1016/j.ijhydene.2026.154563.
[47] Song Z, Zhang R-R, Yan Z-C, Wang J, Liu Y, Jiang C-Q, et al. Porous MXene nanoplatform with ultrahigh drug loading for synergistic photothermal/photodynamic therapy and drug resistance reversal in osteosarcoma. Chem Eng J 2026;534:174971. https://doi.org/10.1016/j.cej.2026.174971.
[48] Yu Z, Lin J, Wang Y, He C, Shi Y, Hu Y, et al. Design, synergistic mechanisms, and application of a MXene@CuS–CeO_2 photothermal–nanozyme multimodal antibacterial material in real water systems. Chem Eng J 2026;532:174295. https://doi.org/10.1016/j.cej.2026.174295.
[49] Guo Z, Mo Y, Li Z, Meng Y, Mei Y, Xie D, et al. Sodium alginate-assisted dispersion of MXene in vulcanization-free natural rubber for efficacy photothermal conversion and electromagnetic shielding. Int J Biol Macromol 2026;344:150322. https://doi.org/10.1016/j.ijbiomac.2026.150322.
[50] Fan S, Tan G, Liu Y, Wu X, Guo L, Zhang B, et al. Pyroelectric-photothermal catalytic CO2 methanation of MXene-based heterojunctions: regulation by local magnetic and local electric field. Separ Purif Technol 2026;393:137255. https://doi.org/10.1016/j.seppur.2026.137255.
[51] Xu K, Tan S, Ye X, Chen M, Xiao Z, Xu T, et al. Chitosan/MXene/carbon nanotube-based phase change materials for integrated photothermal conversion and thermal storage. Chem Eng J 2026;527:172050. https://doi.org/10.1016/j.cej.2025.172050.